Journal of Materials Chemistry C

ROYAL SOCIETY OF CHEMISTRY

PAPER

View Article Online
View Journal | View Issue

Cite this: J. Mater. Chem. C, 2026, 14, 7674

Designing diphosphines towards photo- and electro-luminescent homoleptic Cu(I)/Ag(I) complexes

Sophia Lipinski, [a] Thomas Pickl, [b] Youssef Atoini, [a] Stefano Sansotta, [c] Jean-Louis Schmitt, [d] Luca M. Cavinato, [a] Alexander Pöthig, [b] Julio Fernández-Cestau, [e] Pedro B. Coto *[f] and Rubén D. Costa *[a]

Received 9th February 2026,
Accepted 24th February 2026

DOI: 10.1039/d6tc00433d

rsc.li/materials-c

While luminescent heteroleptic d^{10} complexes have been widely studied, their homoleptic counterparts have been barely explored. Herein, we demonstrate how to tune the emission colour of homoleptic diphosphine Cu(I)/Ag(I) complexes by introducing N-heteroaromatic rings and extended π-systems in the diphosphine backbone (λ_{em} = 455–610 nm). In crystalline powder, photoluminescence quantum yields (PLQYs) of up to 48% and thermally activated delayed fluorescence for both Cu(I) and Ag(I) series were found. However, their photoluminescent behaviour in thin films resulted, for example, in large bathochromically shifted emission maxima and unexpected changes in PLQYs. Besides the presence of aggregation, these findings could also be tentatively attributed to structural distortion of the coordination sphere (*i.e.*, different conformers) upon film formation as suggested by powder X-ray diffraction and theoretical studies. Finally, the best films were also tested in light-emitting electrochemical cells, showing moderate performance, yet comparable to that of devices based on heteroleptic complexes.

Introduction

The development of simple, sustainable, and energy-efficient lighting technologies is crucial to the ongoing transformation of the solid-state lighting sector.[1] In this context, light-emitting electrochemical cells (LECs) are considered as leading example.[2–5] In short, they combine low-cost and up-scalable solution-based fabrication techniques (*e.g.*, spray- and dip-coating) with air-stable electrodes.[6–10] In these devices, the active layer consists of an electroluminescent material – *e.g.*, small molecules,[11–17] ionic transition metal complexes (iTMCs),[3,5,18] perovskites,[19–22] carbon dots,[23–25] and quantum dots[26–31] – blended with an ion-based electrolyte. As the demand for sustainable electroluminescent emitters continues to increase, d^{10}-iTMCs have emerged as non-toxic, eco-friendly, and cost-effective alternatives to their Ir(III) and Ru(II) counterparts.[3,5,32,33] To date, mainly heteroleptic Cu(I) and Ag(I) complexes ($[M(N^N)(P^P)]^+$) with diphosphine (P^P) ligands, such as bis[(2-diphenylphosphino)phenyl] ether (DPEphos) and 4,5-bis(diphenylphosphino)-9,9-dimethyl-9*H*-xanthene (xantphos), as well as diimine (N^N) ligands, *e.g.*, 2,2′-bipyridine, pyridine-pyrazoles and phenanthroline derivatives,[3,5,32,33] have been applied in LECs. The entire visible spectrum can be covered, enabling white-light-emitting devices.[34–45] However, the lighting community identified three major limitations of $[Cu(N^N)(P^P)]^+$ based LECs: (i) severe structural changes in the excited state (Jahn–Teller distortion, formation of penta-coordinated species) that promotes quick degradation (nucleophilic ligand exchange and spontaneous oxidation) upon device fabrication using solvent-based techniques,[3,5,32,33,46–49] (ii) unforeseen changes in the photoluminescent properties when going from powder state to thin-film due to the labile coordination sphere and aggregation,[3,5,32,33] and (iii) irreversible oxidations limiting hole injection and transport under operation.[3,5,32,33] Very recently, attention has been devoted to the photo-/electroluminescent behaviour of heteroleptic $[Ag(N^N)(P^P)]^+$ complexes,

[a] Technical University of Munich, Campus Straubing for Biotechnology and Sustainability, Chair of Biogenic Functional Materials, Schulgasse 22, 94315 Straubing, Germany. E-mail: ruben.costa@tum.de
[b] Technical University of Munich, TUM School of Natural Science, Chair of Inorganic and Metalorganic Chemistry, Lichtenbergstr. 4, 85747 Garching, Germany
[c] Materials Physics Center (CFM)-Spanish National Research Council (CSIC), Paseo Manuel de Lardizabal 5, 20018 Donostia-San Sebastián, Spain
[d] Laboratoire de Chimie Supramoléculaire, Institut de Science et d'Ingénierie Supramoléculaires (ISIS), 8 allée Gaspard Monge, 67083 Strasbourg, France
[e] Universidad de La Rioja, Departamento de Química – Centro de Investigación (CISQ), Madre de Dios 53, 26006 Logroño, Spain
[f] Nanomaterials and Nanotechnology Research Center (CINN), CSIC-University of Oviedo-Principality of Asturias and Donostia International Physics Center (DIPC), Avda. de la Vega 4-6, 33940 El Entrego, Spain. E-mail: pedro.brana@csic.es

encountering different issues. On the one hand, a low electrochemical stability was observed under both reductive and oxidative conditions in solution and devices.[50–52] This could be mitigated by (i) decoupling charge injection/transport and exciton formation in a multilayered device architecture[50] and/or (ii) employing a complex design strategy to enhance the electrochemical stability of heteroleptic Ag(I)-iTMCs.[51] On the other hand, thermally activated delayed fluorescence (TADF) that is typically observed for Cu(I)-iTMCs[3,5,32,33] is rarely encountered for Ag(I)-iTMCs analogues and thus, only a few examples of mononuclear, heteroleptic TADF Ag(I) complexes have been reported.[53–61]

In contrast, phosphorescence originating from ligand-centred (LC) excited states has been more frequently noted for Ag(I)-iTMCs.[51,62,63] In this context, much less attention has been devoted to mononuclear, homoleptic diphosphine Cu(I) and Ag(I) complexes up to date. Actually, a few homoleptic complexes bearing bis(diphenylphosphino)ethane, bis(diphenylphosphino)propane, DPEphos, or bis(diphenylphosphino)-benzene (**dppbz**) are known as high-energy emitters (λ_{em} = 405–505 nm).[61,64–66] Among them, $[M(\mathbf{dppbz})_2]^+$ complexes display the highest photoluminescence quantum yield (PLQY), reaching values of up to 57%.[61,67] Finally, to the best of our knowledge, no homoleptic Cu(I)/Ag(I) complexes have been applied to LECs yet.

Herein, we provide a comprehensive study, in which Cu(I) and Ag(I) were chosen as metal ions and combined with diphosphines of different degrees of electron-withdrawing/π-extended characters going from **dppbz**, over 2,3-bis(diphenylphosphino)-pyrazine (**dpppyrz**), and to 2,3-bis(diphenylphosphino)quinoxaline (**dppquinox**) to generate a series of six homoleptic diphosphine complexes (Scheme 1). This allowed us to disclose three major findings. First, we demonstrate a rational ligand design strategy to cover a broad range of the visible spectrum (λ_{em} = 455–610 nm) in crystalline powder associated with a TADF mechanism regardless of the metal ion. Second, the emission properties in thin-films dramatically change compared to those in crystalline powder. Besides the effect of aggregation, we tentatively point out that these homoleptic complexes might also be prone to distort with respect to the tetrahedral configuration observed in the crystal structures as revealed by powder X-ray diffraction (PXRD), photoluminescence, and theoretical – *i.e.*, density functional theory (DFT) studies. Besides these unforeseen findings, the overall photoluminescence properties were satisfactory enough for some representatives of both families ($\mathbf{M^{bz}}$) to carry out electroluminescence studies in LECs. They showed similar performances regardless of the metal ion, achieving moderate figures-of-merits comparable to the prior art of heteroleptic complexes with similar ligands. All in all, this work highlights the potential of homoleptic Cu(I)/Ag(I) complexes as (i) luminescent materials to cover a broad range of the visible spectrum and (ii) electroluminescent emitters for lighting devices, but also points out their current challenges and limitations.

Results and discussion

Synthesis and structural characterisation

Traditional heteroleptic $[M(P\hat{}P)(N\hat{}N)]^+$ complexes have been based on DPEphos and Xantphos, with the emission wavelengths tailored by tuning the energy levels of the lowest unoccupied molecular orbital (LUMO), primarily located at the N^N ligand.[3,5,32,33] In contrast, this work demonstrates how to modulate the emission features by modifying the electron-withdrawing character of the P^P ligands without drastically changing the steric properties (*e.g.*, bite-angle, ligand buried volume, and ligand flexibility range). In short, the commercially available **dppbz** ligand was selected as reference,[61,64–67] while the central phenyl ring was replaced by electron-withdrawing phenyl derivatives, such as N-heteroaromatic (pyrazine) and π-extended (quinoxaline) systems that led to **dpppyrz** and **dppquinox**, respectively (Scheme 1). The diphosphines **dpppyrz** and **dppquinox** were prepared following a modified procedure from literature[68,69] and characterised by multinuclear NMR spectroscopy (Fig. S1 and S2 and Scheme 2). Specifically, 2,3-dichloropyrazine or 2,3-dichloroquinoxaline suspended in THF was treated with 2.0 eq. of lithium phosphide, $LiPPh_2$, at −78 °C to give the corresponding diphosphine in relatively high yields (70% and 75%, respectively, Scheme 2). The ^{1}H-NMR spectra show the expected downfield shift of the protons located at the phenyl backbone from 6.95/7.15 ppm (**dppbz**) to 8.15 ppm (**dpppyrz**), and to 7.91/7.68 ppm (**dppquinox**), indicating the highest acidity of the protons in the backbone of **dpppyrz**. More importantly, the $^{31}P\{^1H\}$-NMR spectra confirm the introduction of electron-withdrawing groups, with the singlets undergoing a downfield shift from −13.8 ppm (**dppbz**) to −10.4 ppm (**dpppyrz**) and to −9.1 ppm (**dppquinox**), reflecting the reduced electron density on the phosphorus atom (Fig. S1 and S2).

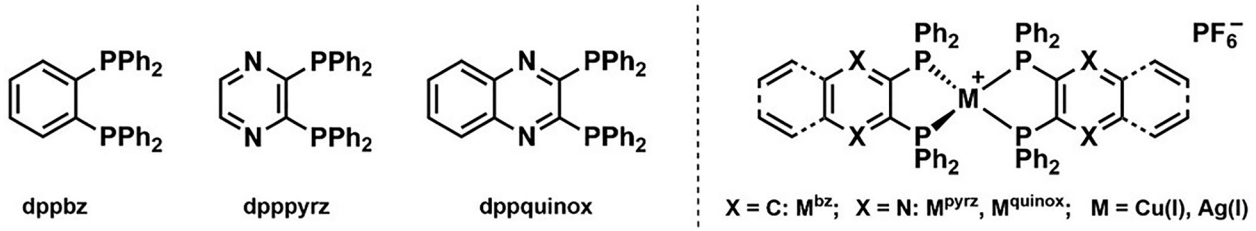

Scheme 1 Molecular structures of **dppbz**, **dpppyrz**, and **dppquinox** ligands (left) and their corresponding homoleptic complexes $\mathbf{M^{bz}}$, $\mathbf{M^{pyrz}}$, and $\mathbf{M^{quinox}}$ (right), M = Cu(I) or Ag(I).

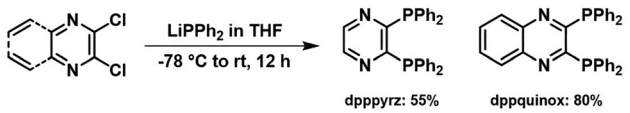

Scheme 2 Synthetic pathway of **dpppyrz** and **dppquinox** ligands.

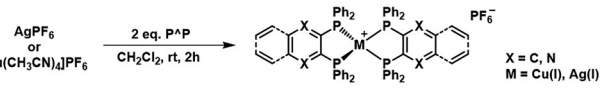

Scheme 3 Preparation of the homoleptic complexes $\mathbf{M^{bz}}$, $\mathbf{M^{pyrz}}$, and $\mathbf{M^{quinox}}$, M = Cu(I) or Ag(I).

The homoleptic Cu(I) and Ag(I) complexes ($[M(P\hat{}P)_2]PF_6$) were synthesized by adding the respective P^P ligands to $[Cu(CH_3CN)_4]PF_6$ or $AgPF_6$ in CH_2Cl_2 (Scheme 3). All six complexes, **$[M(dppbz)_2]PF_6$ (M^{bz})**, **$[M(dpppyrz)_2]PF_6$ (M^{pyrz})**, and **$[M(dppquinox)_2]PF_6$ (M^{quinox})**, were isolated with relatively high yields ranging from 58% to 84% and characterised by ^{1}H-, $^{31}P\{^1H\}$- and $^{13}C\{^1H\}$-NMR as well as electrospray ionisation high-resolution mass spectrometry (ESI-HRMS) that confirmed the presence of the desired mononuclear complex and the absence of di- or polynuclear complexes (Fig. S3–S9). The $^{31}P\{^1H\}$-NMR spectra of $\mathbf{Cu^{bz}}$, $\mathbf{Cu^{pyrz}}$, and $\mathbf{Cu^{quinox}}$ showed the expected broad peaks at δ = 8.17 ppm, 3.80 ppm, and 2.03 ppm due to the electric quadrupole moment of ^{63}Cu and ^{65}Cu (I = 3/2) nuclei,[70] while those of the Ag(I) series exhibited two well resolved doublets owing to the direct coupling of the phosphorus atoms to both spin-active (I = 1/2) silver nuclei ^{107}Ag (52%) and ^{109}Ag (48%).[50,51,70] Finally, the $^{31}P\{^1H\}$-NMR signals of all six complexes undergo a downfield shift relative to the respective free P^P ligands due to the coordination to the metal ion. The relative magnitude of the shift decreases from complexes with **dppbz** to those with **dpppyrz** and **dppquinox**, confirming the progressive increase of their electron-withdrawing character (*vide supra*).

Single crystals suitable for X-ray analysis were obtained by slow diffusion of Et_2O and/or hexane into a highly concentrated solution of $[M(P\hat{}P)_2]PF_6$ in $CDCl_3$ or CD_2Cl_2. The quality of the single crystals of $\mathbf{Cu^{pyrz}}$ was not good enough to obtain a satisfactory crystal structure. The structures of $\mathbf{Ag^{bz}}$ and $\mathbf{Cu^{quinox}}$ are in perfect agreement with those already reported by the groups of Hoshino[66] and Rheingolds,[68] respectively (Fig. S10–S13 and Table S1). Fig. 1 and Fig. S10 and S13 display the structures of, $\mathbf{Ag^{pyrz}}$, $\mathbf{Cu^{bz}}$ and $\mathbf{Ag^{quinox}}$, while selected bond lengths and angles are listed in Table 1, and further crystallographic data are provided in Table S1. In general, the crystal structures of the complexes show a tetrahedral-like coordination with different degrees of distortion, as quantified by the τ_4 parameter.[71] The Cu(I) series is less distorted with τ_4 values of *ca.* 0.80 compared to the Ag(I) series with τ_4 values of *ca.* 0.70 (Table 1). This is expected considering the larger ionic radius of silver (1.29 Å) compared to copper (0.77 Å)[72] that results in smaller bite angles (P1–M–P2/P3–M–P4; Table 1) for the Ag family (*i.e.*, 80.00°/80.00° for $\mathbf{Ag^{bz}}$ to 83.22°/84.33° for $\mathbf{Ag^{pyrz}}$ and 84.07°/80.63° for $\mathbf{Ag^{quinox}}$ *vs.* 84.56°/84.56° for $\mathbf{Cu^{bz}}$ and 90.74°/87.68° for $\mathbf{Cu^{quinox}}$). In addition, longer M–P distances were observed for the Ag(I) series compared to the Cu(I) series, which is in line with the literature (Table 1).[66,68,70] Finally, it is interesting to discuss the C–H–F interactions between the protons of the pyrazine backbone and the PF_6^- anions of $\mathbf{Ag^{pyrz}}$ that range between 1.796 Å and 2.606 Å (Fig. 1). These C–H–F interactions in $\mathbf{Ag^{pyrz}}$ are in good

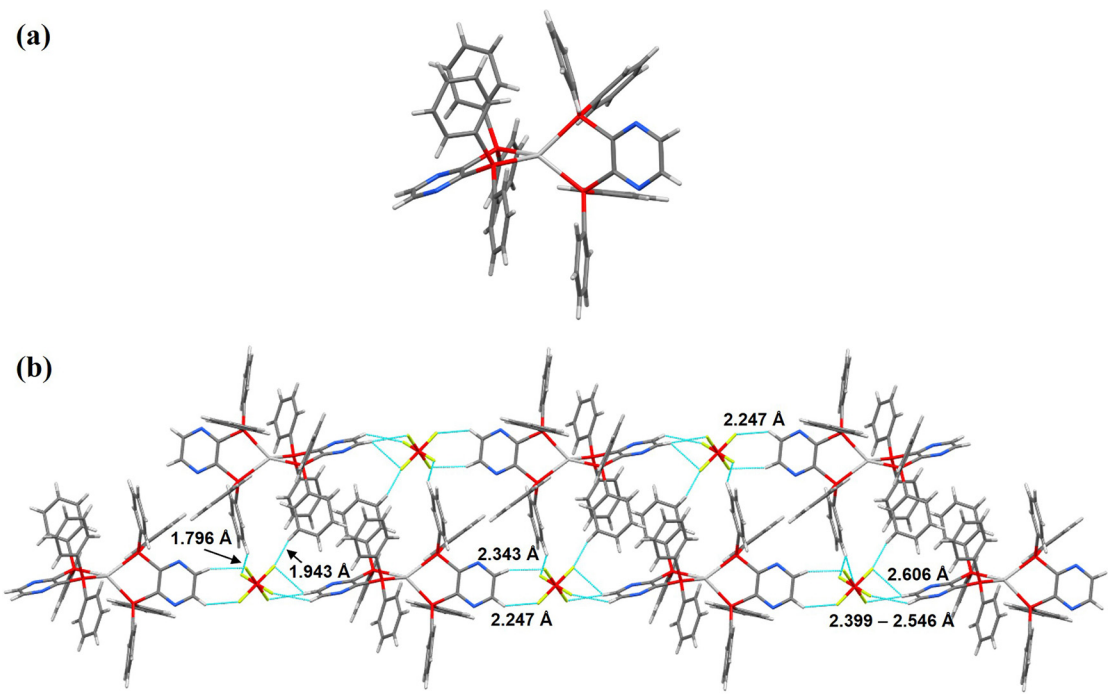

Fig. 1 (a) X-ray structure of $\mathbf{Ag^{pyrz}}$. The PF_6^- anion and solvent molecules are omitted for clarity. (b) View of the short contacts involving the PF_6^- anion in $\mathbf{Ag^{pyrz}}$.

Table 1 Selected bond lengths and angles of $\mathbf{M}^{bz}$, $\mathbf{M}^{pyrz}$ and $\mathbf{M}^{quinox}$

	$\mathbf{Cu}^{bz}$	$\mathbf{Cu}^{quinox,a}$	$\mathbf{Ag}^{bz,b}$	$\mathbf{Ag}^{pyrz}$	$\mathbf{Ag}^{quinox}$
Bond lengths [Å]					
P1–M	2.2925(4)	2.2812(7)	2.4621(7)	2.479(2)	2.4908(10)
P2–M	2.3050(4)	2.2668(7)	2.5063(6)	2.476(2)	2.4612(11)
P3–M	2.2925(4)	2.3152(7)	2.4621(7)	2.474(1)	2.4857(11)
P4–M	2.3051(4)	2.2692(7)	2.5063(6)	2.476(1)	2.5045(10)
Bond angles [°]					
P1–M–P2	84.562(14)	90.74(2)	79.99(2)	83.22(5)	84.08(3)
P1–M–P3	125.71(2)	122.61(3)	133.32(2)	123.79(5)	127.89(4)
P1–M–P4	122.083(14)	114.14(3)	122.25(2)	122.79(5)	114.21(3)
P2–M–P3	122.084(14)	122.54(3)	122.25(2)	122.53(5)	125.43(4)
P2–M–P4	122.86(2)	122.21(3)	125.97(2)	125.52(5)	130.62(4)
P3–M–P4	84.560(14)	87.68(2)	79.99(2)	84.33(5)	80.35(3)
Geometry index					
τ_4	0.79	0.81	0.71	0.79	0.72

[a] Crystal structure data by Hoshino *et al.*[66] [b] Crystal structure data by Rheingolds *et al.*[68]

agreement with the ^{1}H-NMR data, in which the involved hydrogen atoms of the pyrazine backbone feature a downfield shift to 8.78 ppm ($\mathbf{Ag}^{pyrz}$) with respect to, for example, the protons present in their $\mathbf{M}^{bz}$ analogues (Fig. S4–S9). Indeed, the C–H–F interactions in $\mathbf{M}^{bz}$ and $\mathbf{M}^{quinox}$ complexes mainly involve the protons located at the peripheral phenyl groups (Fig. S10–S13).

Electrochemical characterisation

The electrochemical behaviour of the free ligands and the corresponding Cu(I) and Ag(I) complexes was investigated by cyclic voltammetry (CV) in CH_3CN/NBu_4PF_6 (Fig. 2 and Fig. S14 and S15 and Table 2). Both $\mathbf{M}^{bz}$ complexes feature partially reversible oxidations, while multiple irreversible oxidations are noted for those complexes bearing **dpppyrz** and **dppquinox** ligands. In detail, the oxidation potentials of the Cu(I) series are cathodically shifted going from 0.59 V (ΔE = 62.2 mV, i_{pa}/i_{pc} = 7.02; $\mathbf{Cu}^{bz}$), to 0.25 V ($\mathbf{Cu}^{pyrz}$), and to 0.20 V ($\mathbf{Cu}^{quinox}$), while the Ag(I) analogues feature an opposite trend with oxidation waves going from 0.47 V (ΔE = 114 mV, i_{pa}/i_{pc} = 1.59; $\mathbf{Ag}^{bz}$), to 0.50 V ($\mathbf{Ag}^{pyrz}$), and to 0.60 V ($\mathbf{Ag}^{quinox}$). $\mathbf{M}^{bz}$ complexes do not show any reduction in the electrochemical window of CH_3CN, while $\mathbf{M}^{pyrz}$ and $\mathbf{M}^{quinox}$ feature partially reversible reductions. They are anodically shifted, going from $\mathbf{M}^{pyrz}$ to $\mathbf{M}^{quinox}$, with reduction potentials of −1.81 V (ΔE = 81 mV, i_{pa}/i_{pc} = 1.12, $\mathbf{Cu}^{pyrz}$), −1.19 V ($\mathbf{Cu}^{quinox}$), −1.67 V ($\mathbf{Ag}^{pyrz}$), and −1.38 V ($\mathbf{Ag}^{quinox}$).

Finally, repetitive cycles indicate changes in both shapes and potentials of the oxidation/reduction waves for all Ag(I) complexes. This is particularly striking for $\mathbf{Ag}^{pyrz}$ as additional oxidations/reductions evolve (Fig. S15), while no sharp peak at −0.1 V in the anodic scan upon several cycles was noted for all Ag(I) complexes. This suggests the absence of electrochemical formation of Ag(0) as previously noted in heteroleptic Ag(I)-iTMCs.[50–52] Repetitive cycles of the Cu(I) complexes reveal minor changes of the oxidation/reduction waves (Fig. S15). All in all, CV measurements qualitatively confirm the spectroscopic trends (*vide infra*) as well as a slightly different electrochemical behaviour between both homoleptic series. However, this cannot be directly translated to the electrochemical behaviour in thin-films due to the presence of different conformers

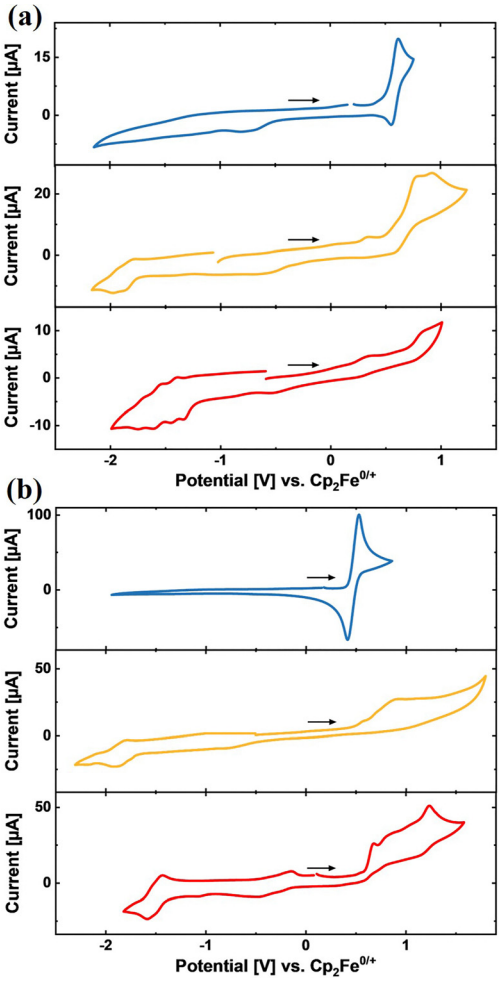

Fig. 2 Cyclic voltammograms (CH_3CN/NBu_4PF_6, 0.1 M, 100 mV s^{-1}, room temperature) of Cu(I) (a) and Ag(I) (b) complexes: $\mathbf{M}^{bz}$ (blue), $\mathbf{M}^{pyrz}$ (yellow) and $\mathbf{M}^{quinox}$ (red) using a Pt working electrode, Pt counter electrode, and Ag wire as quasi-reference electrode.

Table 2 Electrochemical data obtained from CV measurements of $\mathbf{M}^{bz}$, $\mathbf{M}^{pyrz}$ and $\mathbf{M}^{quinox}$ in CH_3CN

	$E_{ox}{}^a$ [V]	$E_{red}{}^a$ [V]
$\mathbf{Cu}^{bz}$	+0.59[b]	—
$\mathbf{Cu}^{pyrz}$	+0.25	−1.81[b]
$\mathbf{Cu}^{quinox}$	+0.20	−1.19
$\mathbf{Ag}^{bz}$	+0.47[b]	—
$\mathbf{Ag}^{pyrz}$	+0.50	−1.67
$\mathbf{Ag}^{quinox}$	+0.60	−1.38

[a] Onset values of the oxidation and reduction are given. [b] Half-wave potential $E_{1/2}$ is given.

(*vide infra*) and the different environment (*e.g.*, complex-complex interactions, lack of solvent effects).

Photophysical and theoretical characterisation

The photoluminescence properties of all complexes were studied in crystalline powder and thin-films before being further used for LECs (*vide infra*; Fig. 3 and Fig. S16 and Table 3).

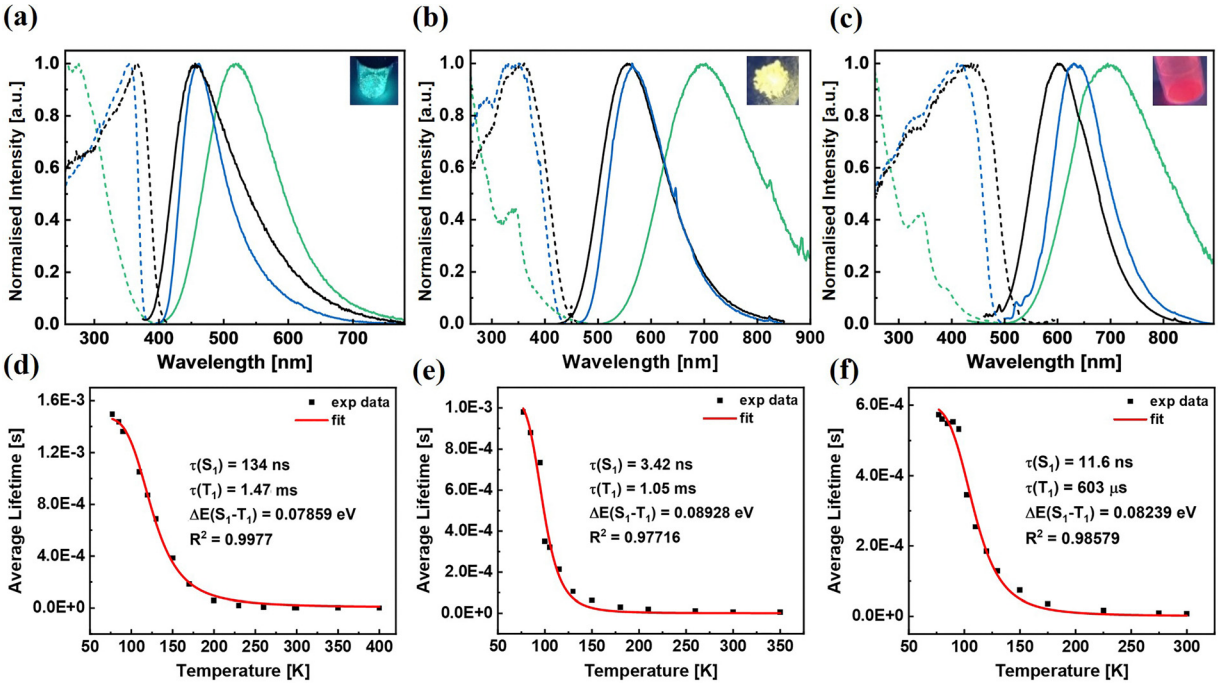

Fig. 3 Top: Excitation (dotted line) and emission (solid line) spectra of Ag^{bz} (a), Ag^{pyrz} (b) and Ag^{quinox} (c) in the crystalline state at 298 K (black), at 77 K (blue) and in thin-films at 298 K (green). Pictures of the crystalline powder under UV irradiation (λ_{ex} = 365 nm, 298 K) are shown as insets. Bottom: Experimental (black) and fitted (red) $\langle\tau\rangle$ *vs.* *T* plots of Ag^{bz} (d), Ag^{pyrz} (e) and Ag^{quinox} (f) in the crystalline powder state.

Table 3 Photophysical properties of M^{bz}, M^{pyrz} and M^{quinox} in crystalline powder and in thin-films at 298 K and 77 K

	$\lambda_{em}/\lambda_{ex}$[a] [nm]	$\langle\tau\rangle$[a] [μs]	ϕ [%]	$\langle k_r\rangle$ × 10^4 [s^{-1}]	$\langle k_{nr}\rangle$ × 10^5 [s^{-1}]	ΔE (S_1-T_1) [meV]	$\lambda_{em}/\lambda_{ex}$[a] [nm]	$\langle\tau\rangle$ [μs]	ϕ [%]	$\langle k_r\rangle$ × 10^4 [s^{-1}]	$\langle k_{nr}\rangle$ × 10^4 [s^{-1}]
	Crystalline powder						Thin-film				
Cu^{bz}	485/360	40.6	48	1.18	1.28	119	515/300	6.23	38	6.1	9.95
	510/360	1.57 × 10^3	—	—	—	—	530/320	1.46 × 10^3	—	—	—
Cu^{pyrz}	557/405	4.03	17	4.33	2.06	77	590/350	12.9	3	0.23	7.52
	560/375	358	—	—	—	—	—	—	—	—	—
Cu^{quinox}	611/420	3.37	2	0.59	2.91	112	—	—	—	—	—
	645/420	1.24 × 10^3	—	—	—	—					
Ag^{bz}	455/360	5.49	23	4.19	1.4	78.5	522/345	8.53	45	5.63	6.1
	460/350	1.50 × 10^3	—	—	—	—	506/345	625	—	—	—
Ag^{pyrz}	555/365	6.61	13	3.48	1.32	89.3	700/350	0.8	< 1	—	—
	565/400	980	—	—	—	—	—	—	—	—	—
Ag^{quinox}	605/400	7.71	6	77.8	1.22	82.4	695/390	0.85	2	2.35	1.15
	635/400	572	—	—	—	—	690/400[b]	0.72[b]	< 1[b]	—	—

[a] Top values recorded at 298 K, bottom values recorded at 77 K. [b] Values obtained for the amorphous powder.

Unfortunately, the complexes are not emissive in solution, showing at best PLQYs <0.2%, while they are good emitters in crystalline powder. The photoluminescence behaviour of Cu^{bz}, Cu^{pyrz}, and Cu^{quinox} in crystalline powder is characterised by a broad emission band centred at 485 nm, 555 nm, and 611 nm associated with average excited-state lifetimes $\langle\tau\rangle$/PLQYs values of 40.6 μs/48%, 4.03 μs/17%, and 3.37 μs/2%, respectively. Likewise, the Ag(I) complexes show similar broad emission bands peaking at 455 nm, 555 nm, and 605 nm with $\langle\tau\rangle$/PLQYs values of 5.49 μs/23%, 6.61 μs/13%, and 7.71 μs/6% for Ag^{bz}, Ag^{pyrz}, and Ag^{quinox}, respectively. In line with the electrochemical data, the maximum of the emission wavelength is red-shifted from **dppbz**, **dpppyrz**, and **dppquinox**, while the reduction of the PLQYs is expected by the energy gap law.[73] In addition, the broad emission band shape typically suggests a metal-to-ligand (MLCT) and/or ligand-to-ligand charge transfer (LLCT) character (Fig. S17 and S18 and Tables S2 and S3).

To determine the nature of the emitting states in both families, the equilibrium structures of their lowest-lying singlet and triplet excited states were calculated using time-dependent DFT (TDDFT) (SI). In detail, we found equilibrium structures for S_1 and T_1 whose conformations are close to those found for the complexes in the crystal (*i.e.*, with a tetrahedral-like

arrangement of the ligands around the metal centre; Fig. S17–S18 and Tables S2 and S3). The results indicate that both S_1 and T_1 exhibit a similar character in both Cu(I) and Ag(I) complexes with a dominant HOMO→LUMO like single excitation (SI). The HOMO exhibits a semi-localised character showing a mixture of metal and diphosphine ligand contributions, while the LUMO is a π*-like orbital localised on one of the **dppbz**, **dpppyrz**, and **dppquinox** moieties (Fig. S17 and S18), suggesting charge transfer character of the emitting excited state. However, the T_1 states of $\mathbf{Cu^{quinox}}$ and $\mathbf{Ag^{quinox}}$ exhibit a more mixed character dominated by an intraligand π → π* transition. Since the emission mechanism might be related to either phosphorescence or TADF, temperature-dependent photoluminescence studies (*i.e.*, changes in the emission spectrum and $\langle\tau\rangle$ in the range from 77 K to 350 K) were carried out. In line with previous works by Yersin and co-workers,[67] we also found TADF as the main emissive pathway for $\mathbf{Cu^{bz}}$ at room temperature ($\Delta E(S_1–T_1)$ = 119 meV, Fig. S16). Similarly, $\mathbf{Cu^{pyrz}}$ and $\mathbf{Cu^{quinox}}$ showed the characteristic TADF behaviour in the crystalline powder state (Fig. S16 and Table 3). Upon cooling to 77 K, a distinct redshift of the E_{0-0} band is noted for $\mathbf{Cu^{pyrz}}$ and $\mathbf{Cu^{quinox}}$, accompanied by a drastic increase in $\langle\tau\rangle$ from 4.03 μs and 3.37 μs at 298 K to 358 μs and 1.24 ms at 77 K, respectively. This is indicative of a change in the decay path to the spin-forbidden $T_1 \rightarrow S_0$ transition (phosphorescence). A further increase in temperature leads to a sharp drop of $\langle\tau\rangle$ around 100 K, suggesting the thermal population of the higher-lying S_1 state from the T_1 state *via* reverse intersystem crossing (rISC). At 170 K ($\mathbf{Cu^{pyrz}}$) and 210 K ($\mathbf{Cu^{quinox}}$) a plateau is reached as TADF dominates the emissive pathway over phosphorescence. Typically, the temperature dependence of $\langle\tau\rangle$ *vs.* T is fitted with the two-state Boltzmann model, assuming fast thermal equilibration between the T_1 and S_1 states (SI). The obtained splitting energies between singlet and triplet states of 77.0 meV ($\mathbf{Cu^{pyrz}}$) and 112 meV ($\mathbf{Cu^{quinox}}$) are in the expected range for efficient Cu(I) TADF emitters.[3,5,32,33]

In contrast to the prior art of heteroleptic Ag(I)-iTMCs,[3,5,32,33] the homoleptic Ag(I) series shows a TADF behaviour similar to their Cu(I) analogues. Upon cooling to 77 K, all three Ag(I) complexes show the typical red-shifted E_{0-0} band and/or emission maxima accompanied by slightly narrowed emission bands (Fig. 3 and Table 3). The $\langle\tau\rangle$ increases significantly to 1.47 ms ($\mathbf{Ag^{bz}}$), 927 μs ($\mathbf{Ag^{pyrz}}$), and 572 μs ($\mathbf{Ag^{quinox}}$) compared to 5.49 μs, 6.61 μs, and 7.71 μs at 298 K. An increase in temperature leads to the expected drop of $\langle\tau\rangle$ at 110 K ($\mathbf{Ag^{bz}}$), 80 K ($\mathbf{Ag^{pyrz}}$), and 100 K ($\mathbf{Ag^{quinox}}$), suggesting the beginning of the population of the S_1 state from the T_1 state. From 220 K ($\mathbf{Ag^{bz}}$), 160 K ($\mathbf{Ag^{pyrz}}$), and 170 K ($\mathbf{Ag^{quinox}}$) on, TADF dominates the emission as evidenced by the presence of a plateau. Like the Cu(I) analogues, $\Delta E(S_1–T_1)$ values were estimated to be 78.5 meV ($\mathbf{Ag^{bz}}$), 89.3 meV ($\mathbf{Ag^{pyrz}}$), and 82.4 meV ($\mathbf{Ag^{quinox}}$) using the two-state Boltzmann-type equation. These findings were further supported by TDDFT studies (SI). In all these cases, we have found vertical emission energies (VEE) and adiabatic singlet–triplet energy differences $\Delta E(S_1–T_1)$ that are in reasonable agreement with the experimentally observed TADF behaviour.

Concerning the emission properties, the VEE energies of S_1 and T_1 for the different complexes are, in general, in agreement with the experimental data, differing by $\lesssim$0.2 eV (Fig. S17 and Table S2). In conjunction with the experimental $\langle\tau\rangle$ values, we tentatively assign the room temperature emission to the S_1 state (high-energy emission) and the emission at 77 K to the T_1 state (low-energy emission), confirming the plausible TADF mechanism although the calculated adiabatic $\Delta E(S_1–T_1)$ values of 0.21 eV, 0.13 eV, and 0.29 eV for $\mathbf{Cu^{bz}}$, $\mathbf{Cu^{pyrz}}$, and $\mathbf{Cu^{quinox}}$, respectively, and 0.24 eV, 0.07 eV, and 0.24 eV for the corresponding Ag(I) analogues, $\mathbf{Ag^{bz}}$, $\mathbf{Ag^{pyrz}}$, and $\mathbf{Ag^{quinox}}$, are larger than those experimentally found (SI). These discrepancies can be explained by the limitations of the model, as it does not take into account, among others, the long-range interactions existing in the crystalline powder and the effect of the counterions present in the crystal.

Next, we turned our attention to the thin-films prepared by spin-coating that will be further applied to LECs (SI). The homogeneous and pin-hole free morphology was confirmed using atomic force microscopy (AFM), showing roughness factors ranging from 207 pm to 3.69 nm (Fig. S19). Unexpectedly, the emission properties of the thin-films changed dramatically compared to those in crystalline powder. In detail, the emission maxima are significantly red-shifted (*i.e.*, $\Delta\lambda_{em}$ ranging from 30 nm to 145 nm, Table 3), accompanied by a strong broadening of the emission bands (*i.e.*, increase of full-width half maximum (FWHM) of 20 nm to 90 nm), while $\mathbf{Cu^{quinox}}$ is not emissive (Fig. 3, S20 and Table 3). This goes hand-in-hand with a further reduction of the PLQY values down to 38% and 3% for $\mathbf{Cu^{bz}}$ and $\mathbf{Cu^{pyrz}}$, as well as <1 and 2% for $\mathbf{Ag^{pyrz}}$ and $\mathbf{Ag^{quinox}}$, while the $\langle\tau\rangle$ values remain in the μs range. In contrast, $\mathbf{Ag^{bz}}$ shows an increase in the PLQY and $\langle\tau\rangle$ values compared to those in crystalline powder (thin-film *vs.* crystalline powder: 45% *vs.* 23%; 8.5 μs *vs.* 5.5 μs). These changes when going from powder to solvent-processed thin-films might be related to aggregation and/or distortion of the coordination sphere, as discussed in the literature for Cu(I)-iTMCs.[3,5,32,33] Specifically in Ag(I) complexes, Osawa *et al.* and Matsumoto *et al.* have also reported a change from tetrahedral to quasi square-planar geometry upon exciting $\mathbf{Ag^{bz}}$ in solution,[64,66] while this has been barely studied in thin-films. Thus, a joint theoretical and experimental study was carried out to better understand these findings. As a first hint, we attempted to prepare amorphous powder samples for all the complexes by quick solvent evaporation under high vacuum, but most of the complexes still showed a mixture of crystalline and amorphous features, as shown in the PXRD pattern (Fig. S21). Fortunately, the PXRD pattern of $\mathbf{Ag^{quinox}}$ showed no crystalline features (Fig. 4). Here, the emission maximum is significantly red-shifted compared to that of the crystalline powder, and it resembles that of the thin-films (Fig. 4 and Table 3). Furthermore, temperature-dependent photoluminescence studies were carried out for $\mathbf{Cu^{bz}}$ and $\mathbf{Ag^{bz}}$ as the best candidates for LECs. $\mathbf{Cu^{bz}}$ showed TADF similar to that exhibited in powder. Upon cooling to 77 K, a bathochromic shift of the emission maximum accompanied by a slightly narrowed band was observed

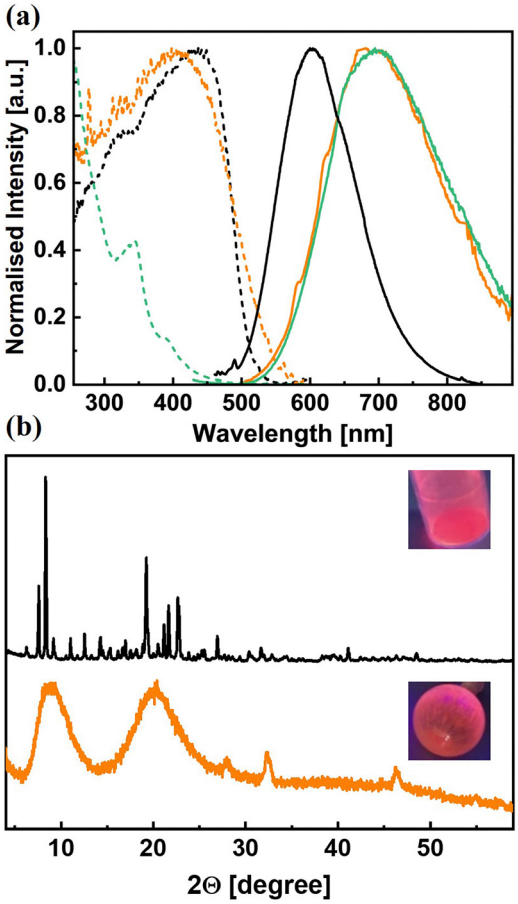

Fig. 4 (a) Excitation (dotted line) and emission (solid line) spectra of Ag^{quinox} in the crystalline powder (black), amorphous (orange) state, and thin-films (green). (b) PXRD patterns of Ag^{quinox} of the crystalline (black) and amorphous (orange) sample. Pictures of the crystalline and amorphous samples under UV irradiation (λ_{ex} = 365 nm, 298 K) are shown as insets.

(Fig. S20 and Table 3). The $\langle\tau\rangle$ values increased drastically from 40.6 μs at room temperature to 1.44 ms at 77 K. An increase in temperature up to 300 K led to the typical $\langle\tau\rangle$ *vs.* T profile obtained for TADF emitters. However, the temperature dependence of $\langle\tau\rangle$ could not be fitted with the two-state Boltzmann-type equation. This issue was already encountered by Yersin *et al.* who related it to the presence of different conformations, resulting in multiple decay components that hamper a reasonable fitting.[67,74] Contrary to the behaviour of Ag^{bz} crystalline powder and Cu^{bz} films, Ag^{bz} films showed a distinct blue-shift of the maximum emission wavelength upon cooling to 77 K, but also an increase of $\langle\tau\rangle$ from 8.53 μs at room temperature to 625 μs at 77 K (Fig. S20 and Table 3). The $\langle\tau\rangle$ *vs.* T plot again exhibited the typical behaviour expected for a TADF emitter, but we did not succeed in fitting it with the two-state Boltzmann-type equation. Based on the above findings, we conclude that the existence of different conformations in the thin-films and the complex environment, in which they are embedded, prevents an unambiguous assignment of the emission mechanism in thin-film.

To gain more insights into the complex interplay between distortions in the coordination sphere and the nature of the emitting electronic excited states in thin-films, we theoretically characterised the impact of conformational changes on the emission features of the complexes. Indeed, our results show the existence of several stable conformations that differ in the arrangement of the **dppbz**, **dpppyrz**, and **dppquinox** ligands around the metal centre. Their different S_1 and T_1 conformations as well as their emission properties were calculated (SI). In short, we have found distorted tetrahedral-like structures, where the **dppbz**, **dpppyrz**, and **dppquinox** moieties are twisted with respect to the conformation found in the crystal structure (Fig. S17 and Table S3). In general, the VEE of S_1 and T_1 for these distorted conformations are red-shifted with respect to the values found for the tetrahedral, crystal-like structures which are in line with the experimental results found for the thin-films. Comparison of these values with the experimental thin-film emission energies shows larger discrepancies than those noted for the crystalline powder but also reveals a trend that is in reasonable agreement with the experimental data (Table S3). In this context, it is important to note that the local environment in the thin-films is not considered in our model. Nevertheless, the S_1 and T_1 distorted structures exhibit an adiabatic $\Delta E(S_1–T_1)$ value that could be consistent with a TADF mechanism (SI), as also suggested by the above spectroscopic findings.

Electroluminescence studies in LECs

LECs were prepared by spin coating an 80 nm layer of poly(3,4-ethylene-dioxythiophene):polystyrene sulfonate (PEDOT:PSS) on a glass substrate coated with indium tin oxide (ITO), followed by the active layer (75 nm to 90 nm) spin coated from a CH_3CN solution of the best emitters, Cu^{bz} and Ag^{bz}, respectively. The Al cathode (100 nm) was deposited onto the active layer by physical vapour deposition (SI). The devices were driven at a pulsed current of 15 mA with a driving scheme based on a block wave at 1000 Hz and a duty cycle of 50%. All devices feature the typical LEC behaviour, highlighted by the voltage decay due to the formation of the electric double layers (EDLs) at the electrode interface until reaching a constant plateau (Fig. 5).[75] As far as the brightness is concerned, Cu^{bz}- and Ag^{bz}-LECs feature an emission response with an emission band centred at 550 nm and 540 nm associated with maximum luminance (L_{max}) of 6.9 cd m^{-2} and 3.2 cd m^{-2} and maxima efficiencies of 0.014 cd A^{-1} and 0.006 cd A^{-1}, respectively (Fig. 5). Compared to the photoluminescence spectra of Cu^{bz} and Ag^{bz} in thin-films, the initial electroluminescence spectra are red-shifted (~30 nm), which is consistent with polarization effects (Fig. 5). This indicates that the same emitting excited states might be involved regardless of the external stimuli (*i.e.*, electrical and/or irradiation). Finally, the electroluminescence spectra undergo a progressive red shift of their emission wavelength maxima over time, which is related to dynamic changes in the neutral emitting zone (i) over time as the growth of the doped regions evolves. This results in (i) a width reduction of the emitting zone, leading to exciton-polaron

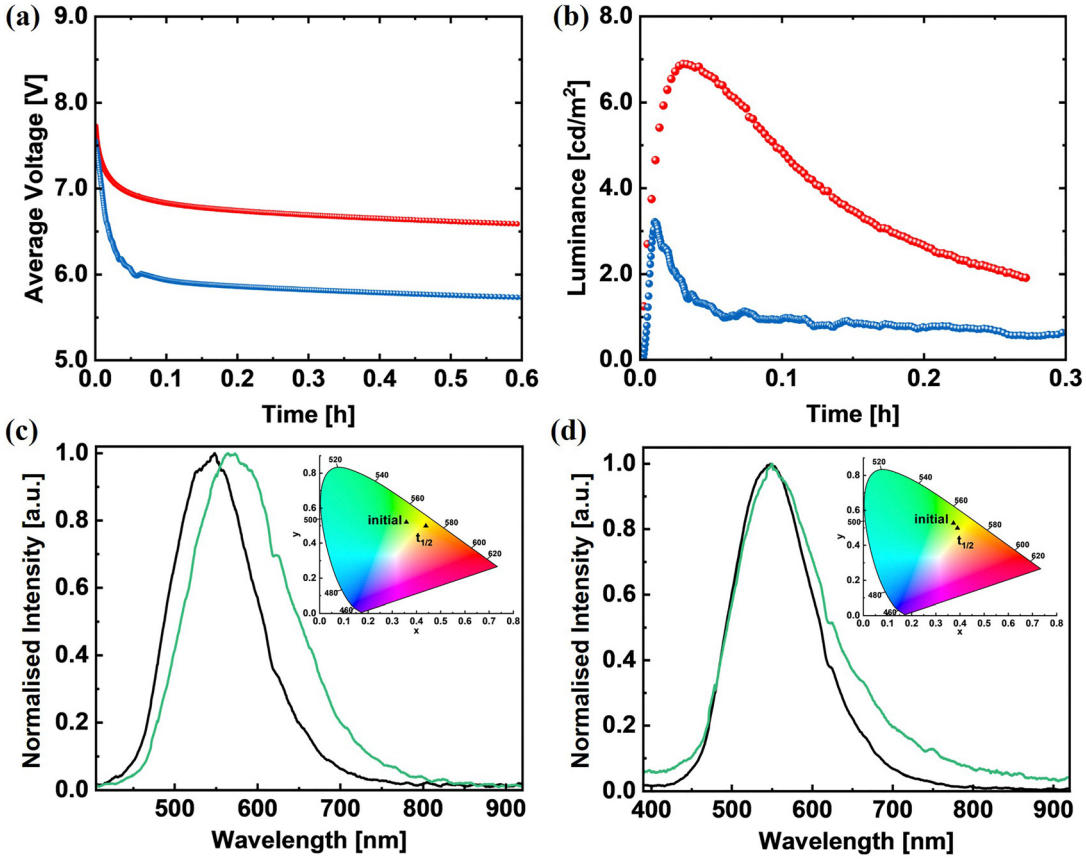

Fig. 5 Top: (a) Average voltage and (b) luminance of $\mathbf{Cu^{bz}}$- (red) and $\mathbf{Ag^{bz}}$-LEC (blue) *vs.* time – driven at pulsed current of 15 mA using ITO/PEDOT:PSS/$\mathbf{M^{bz}}$/Al device architecture. Bottom: Initial (black) and half-life (green) electroluminescence spectrum with the *x*/*y* CIE colour coordinates as insets of $\mathbf{Cu^{bz}}$- (c) and $\mathbf{Ag^{bz}}$-LECs (d).

emission quenching that slowly reduces the device brightness, reaching device stabilities of <0.2 h, and (ii) a microcavity effect red-shifting the device chromaticity.[76]

Conclusions

This work presents a family of homoleptic Cu(I) and Ag(I) complexes bearing chelating 1,2-bis(diphenylphosphino)-functionalised phenyl derivatives. The systematic introduction of electron-withdrawing groups in the diphosphine backbone without affecting the steric properties enabled emission colours of the corresponding complexes in a wide range of the visible spectrum (λ_{em} = 455–610 nm). A temperature-dependent emission study in conjunction with theoretical calculations (DFT/TDDFT) provides evidence for TADF in the crystalline powder for both Cu(I) and Ag(I) series. This is particularly interesting for the Ag(I) series, since their heteroleptic counterparts mainly show phosphorescence and only few examples of Ag(I) complexes showing TADF have been reported so far. A dramatic change in the photoluminescence in thin-films associated with large emission shifts as well as a complex temperature-dependent emission behaviour does not allow us to unambiguously determine the emission mechanism. While these changes could be related to aggregation, we also highlight in this work that the presence of different conformers caused by the structural distortions of the labile coordination sphere upon film formation should be considered as well. This is supported by theoretical studies, in which distorted tetrahedral-like conformations compared to the ones in the single crystals were found to be in a reasonable agreement with the photoluminescence behaviour in thin-films. To confirm these findings, the structure of these conformers should be determined by, for example, synchrotron analysis coupled with X-ray absorption/emission spectroscopy of thin-films. Besides, the photoluminescence features of $\mathbf{Cu^{bz}}$ and $\mathbf{Ag^{bz}}$ in thin-films were good enough to study their electroluminescence in LECs that show moderate performances yet comparable to the prior-art LECs based on heteroleptic d^{10} complexes. Overall, this work presents a systematic study of homoleptic Cu(I)/Ag(I) complexes, revealing their potential as emitters, but also the challenges concerning the need for a more robust design of the coordination sphere for thin-film lighting applications.

Author contributions

S. L. performed the synthesis, characterisation and formal analysis of both series, photophysical and electrochemical experiments and formal analysis, as well as the device

preparation, characterisation, and formal analysis. S. L. also wrote the manuscript. R. D. C was responsible for the conceptualization and funding. T. P., A. P. and J. F.-C. measured and solved the single X-ray structures. J.-L. S. carried out the mass spectroscopy and formal analysis. Y. A. performed the PXRD measurements and assisted in the synthesis, spectroscopy characterisations and formal analysis. L. M. C. carried out AFM characterisation and formal analysis. S. S. and P. B. C. performed the DFT and TDDFT calculations and formal analysis. J. F.-C. and Y. A. carried out supervision. All authors have revised the manuscript and given their approval to the final version.

Conflicts of interest

There are no conflicts to declare.

Data availability

Detailed synthetic procedures for all compounds, additional photophysical data (steady-state spectra, $\langle\tau\rangle$ *versus* T plots), additional electrochemical measurements as mentioned in the text, X-ray data, DFT/TDDFT data, and multinuclear NMR and HRMS spectra for all compounds (pdf).

CCDC 2406496 ($\mathbf{Cu^{bz}}$), 2425241 ($\mathbf{Ag^{pyrz}}$), 2406497 ($\mathbf{Ag^{quinox}}$) contain the supplementary crystallographic data for this paper.[77a–c]

Supplementary information (SI) is available. See DOI: https://doi.org/10.1039/d6tc00433d.

Acknowledgements

We are thankful to Technical University of Munich for generous funding. J. F.-C holds a Ramón y Cajal Fellowship (RYC2021-034075-I) and is funded by MCIN/AEI/10.13039/501100011033 and the European Union ''NextGenerationEU/PRTR''.

Notes and references

1 ed. H. Yersin, *Highly Efficient OLEDs*, Wiley-VCH Verlag GmbH & Co. KGaA, Weinheim, Germany, 2018.
2 E. Fresta and R. D. Costa, *J. Mater. Chem. C*, 2017, **5**, 5643–5675.
3 A. Farokhi, S. Lipinski, L. M. Cavinato, H. Shahroosvand, B. Pashaei, S. Karimi, S. Bellani, F. Bonaccorso and R. D. Costa, *Chem. Soc. Rev.*, 2025, **54**, 266–340.
4 E. Fresta and R. D. Costa, *Adv. Funct. Mater.*, 2020, **30**, 1908176.
5 G. U. Mahoro, J. Fernandez-Cestau, J.-L. Renaud, P. B. Coto, R. D. Costa and S. Gaillard, *Adv. Opt. Mater.*, 2020, **8**, 2000260.
6 M. Pietsch, N. Casado, D. Mecerreyes and G. Hernandez-Sosa, *ACS Appl. Mater. Interfaces*, 2022, **14**, 43568–43575.
7 M. Pietsch, T. Rödlmeier, S. Schlisske, J. Zimmermann, C. Romero-Nieto and G. Hernandez-Sosa, *J. Mater. Chem. C*, 2019, **7**, 7121–7127.
8 A. Sandström, A. Asadpoordarvish, J. Enevold and L. Edman, *Adv. Mater.*, 2014, **26**, 4975–4980.
9 E. M. Lindh, A. Sandström and L. Edman, *Small*, 2014, **10**, 4148–4153.
10 S. Tang, A. Sandström, P. Lundberg, T. Lanz, C. Larsen, S. van Reenen, M. Kemerink and L. Edman, *Nat. Commun.*, 2017, **8**, 1190.
11 S. Kanagaraj, A. Puthanveedu and Y. Choe, *Adv. Funct. Mater.*, 2020, **30**, 1907126.
12 A. Sanz-Velasco, O. Amargós-Reyes, A. Kähäri, S. Lipinski, L. M. Cavinato, R. D. Costa, M. A. Kostiainen and E. Anaya-Plaza, *Chem. Sci.*, 2024, **15**, 2755–2762.
13 S. Tang, P. Lundberg, Y. Tsuchiya, J. Ràfols-Ribé, Y. Liu, J. Wang, C. Adachi and L. Edman, *Adv. Funct. Mater.*, 2022, **32**, 2205967.
14 J. C. John, K. Shanmugasundaram, G. Gopakumar and Y. Choe, *ACS Photonics*, 2022, **9**, 203–210.
15 J. C. John, K. Shanmugasundaram, C. V. S. Brahmmananda Rao, G. Gopakumar and Y. Choe, *J. Phys. Chem. C*, 2021, **125**, 17993–18001.
16 L. M. Cavinato, K. Yamaoka, S. Lipinski, V. Calvi, D. Wehenkel, R. van Rijn, K. Albrecht and R. D. Costa, *Adv. Funct. Mater.*, 2023, **33**, 2302483.
17 K. Matsuki, J. Pu and T. Takenobu, *Adv. Funct. Mater.*, 2020, **30**, 1908641.
18 R. Bai, X. Meng, X. Wang and L. He, *Adv. Funct. Mater.*, 2020, **30**, 1907169.
19 A. Mishra, M. Alahbakhshi, R. Haroldson, L. D. Bastatas, Q. Gu, A. A. Zakhidov and J. D. Slinker, *Adv. Opt. Mater.*, 2020, **8**, 2000226.
20 A. Mishra, M. Alahbakhshi, R. Haroldson, Q. Gu, A. A. Zakhidov and J. D. Slinker, *Adv. Funct. Mater.*, 2021, **31**, 2102006.
21 D. Gets, M. Alahbakhshi, A. Mishra, R. Haroldson, A. Papadimitratos, A. Ishteev, D. Saranin, S. Anoshkin, A. Pushkarev, E. Danilovskiy, S. Makarov, J. D. Slinker and A. A. Zakhidov, *Adv. Opt. Mater.*, 2021, **9**, 2001715.
22 W.-L. Kang, Y.-T. Tsai, Y.-C. Ji, R.-H. Yi, Y.-X. Wang, H.-L. Shen, X.-J. Chen, Y.-C. Hsu, C.-W. Lu, Z.-P. Yang and H.-C. Su, *Chem. – Eur. J.*, 2021, **27**, 17785–17793.
23 Y. Liu, S. Tang, X. Wu, N. Boulanger, E. Gracia-Espino, T. Wågberg, L. Edman and J. Wang, *Nano Res.*, 2022, **15**, 5610–5618.
24 S. Tang, Y. Liu, H. Opoku, M. Gregorsson, P. Zhang, E. Auroux, D. Dang, A.-V. Mudring, T. Wågberg, L. Edman and J. Wang, *Green Chem.*, 2023, **25**, 9884–9895.
25 L. M. Cavinato, V. Kost, S. Campos-Jara, S. Ferrara, S. Chowdhury, I. M. Groot, T. Da Ros and R. D. Costa, *Adv. Opt. Mater.*, 2024, **12**, 2400618.
26 E. Nannen, J. Frohleiks and S. Gellner, *Adv. Funct. Mater.*, 2020, **30**, 1907349.
27 S. Park, J. Yang, S. Kim, D. Hahm, H. Jo, W. K. Bae and M. S. Kang, *Adv. Opt. Mater.*, 2020, **8**, 2001535.
28 H. Chen, R. F. Ubbink, R. A. Olsthoorn, M. Stam, J. 't Hoen, T. J. Savenije and A. J. Houtepen, *Chem. Mater.*, 2025, **37**, 4435–4444.

29 J. Frohleiks, S. Gellner, S. Wepfer, G. Bacher and E. Nannen, *ACS Appl. Mater. Interfaces*, 2018, **10**, 42637–42646.
30 J. Frohleiks, S. Wepfer, Y. Kelestemur, H. V. Demir, G. Bacher and E. Nannen, *ACS Appl. Mater. Interfaces*, 2016, **8**, 24692–24698.
31 Y.-H. Tang, Y.-C. Chiu, D. Luo, J.-Y. Lien, R.-H. Yi, C.-H. Lin, Z.-P. Yang, C.-W. Lu and H.-C. Su, *Chem. – Eur. J.*, 2020, **26**, 13668–13676.
32 V. Ferraro, C. Bizzarri and S. Bräse, *Adv. Sci.*, 2024, **11**, e2404866.
33 C. E. Housecroft and E. C. Constable, *J. Mater. Chem. C*, 2022, **10**, 4456–4482.
34 C. Li, C. F. R. Mackenzie, S. A. Said, A. K. Pal, M. A. Haghighatbin, A. Babaei, M. Sessolo, D. B. Cordes, A. M. Z. Slawin, P. C. J. Kamer, H. J. Bolink, C. F. Hogan and E. Zysman-Colman, *Inorg. Chem.*, 2021, **60**, 10323–10339.
35 L. M. Cavinato, S. Wölfl, A. Pöthig, E. Fresta, C. Garino, J. Fernandez-Cestau, C. Barolo and R. D. Costa, *Adv. Mater.*, 2022, **34**, e2109228.
36 S. Keller, E. C. Constable, C. E. Housecroft, M. Neuburger, A. Prescimone, G. Longo, A. Pertegás, M. Sessolo and H. J. Bolink, *Dalton Trans.*, 2014, **43**, 16593–16596.
37 S. Keller, A. Pertegás, G. Longo, L. Martínez, J. Cerdá, J. M. Junquera-Hernández, A. Prescimone, E. C. Constable, C. E. Housecroft, E. Ortí and H. J. Bolink, *J. Mater. Chem. C*, 2016, **4**, 3857–3871.
38 S. Keller, A. Prescimone, H. Bolink, M. Sessolo, G. Longo, L. Martínez-Sarti, J. M. Junquera-Hernández, E. C. Constable, E. Ortí and C. E. Housecroft, *Dalton Trans.*, 2018, **47**, 14263–14276.
39 A. Jouaiti, L. Ballerini, H.-L. Shen, R. Viel, F. Polo, N. Kyritsakas, S. Haacke, Y.-T. Huang, C.-W. Lu, C. Gourlaouen, H.-C. Su and M. Mauro, *Angew. Chem., Int. Ed.*, 2023, **62**, e202305569.
40 B. Hupp, C. Schiller, C. Lenczyk, M. Stanoppi, K. Edkins, A. Lorbach and A. Steffen, *Inorg. Chem.*, 2017, **56**, 8996–9008.
41 R. Czerwieniec, J. Yu and H. Yersin, *Inorg. Chem.*, 2011, **50**, 8293–8301.
42 E. Fresta, G. U. Mahoro, L. M. Cavinato, J.-F. Lohier, J.-L. Renaud, S. Gaillard and R. D. Costa, *Adv. Opt. Mater.*, 2022, **10**, 2101999.
43 G. U. Mahoro, E. Fresta, M. Elie, D. Di Nasso, Q. Zhang, J.-F. Lohier, J.-L. Renaud, M. Linares, R. Wannemacher, J. Cabanillas-Gonzalez, R. D. Costa and S. Gaillard, *Dalton Trans.*, 2021, **50**, 11049–11060.
44 E. Fresta, G. Volpi, M. Milanesio, C. Garino, C. Barolo and R. D. Costa, *Inorg. Chem.*, 2018, **57**, 10469–10479.
45 E. Fresta, M. D. Weber, J. Fernandez-Cestau and R. D. Costa, *Adv. Opt. Mater.*, 2019, **7**, 1900830.
46 C. Förster and K. Heinze, *Chem. Soc. Rev.*, 2020, **49**, 1057–1070.
47 S. Garakyaraghi, E. O. Danilov, C. E. McCusker and F. N. Castellano, *J. Phys. Chem. A*, 2015, **119**, 3181–3193.
48 M. Iwamura, S. Takeuchi and T. Tahara, *Acc. Chem. Res.*, 2015, **48**, 782–791.
49 M. W. Mara, K. A. Fransted and L. X. Chen, *Coord. Chem. Rev.*, 2015, **282–283**, 2–18.
50 E. Fresta, J. M. Carbonell-Vilar, J. Yu, D. Armentano, J. Cano, M. Viciano-Chumillas and R. D. Costa, *Adv. Funct. Mater.*, 2019, **29**, 1901797.
51 S. Lipinski, L. M. Cavinato, T. Pickl, G. Biffi, A. Pöthig, P. B. Coto, J. Fernández-Cestau and R. D. Costa, *Adv. Opt. Mater.*, 2023, **11**, 2203145.
52 B. Nemati Bideh, H. Shahroosvand and M. K. Nazeeruddin, *Inorg. Chem.*, 2021, **60**, 11915–11922.
53 M. Klein, N. Rau, M. Wende, J. Sundermeyer, G. Cheng, C.-M. Che, A. Schinabeck and H. Yersin, *Chem. Mater.*, 2020, **32**, 10365–10382.
54 M. Z. Shafikov, A. F. Suleymanova, R. Czerwieniec and H. Yersin, *Inorg. Chem.*, 2017, **56**, 13274–13285.
55 M. Z. Shafikov, A. F. Suleymanova, R. Czerwieniec and H. Yersin, *Chem. Mater.*, 2017, **29**, 1708–1715.
56 T. Teng, K. Li, G. Cheng, Y. Wang, J. Wang, J. Li, C. Zhou, H. Liu, T. Zou, J. Xiong, C. Wu, H.-X. Zhang, C.-M. Che and C. Yang, *Inorg. Chem.*, 2020, **59**, 12122–12131.
57 X.-B. Cai, D. Liang, D.-C. Zhang, J.-H. Jia, X.-Y. Wu and C.-Z. Lu, *Chem. Sci.*, 2025, **16**, 9802–9808.
58 D. Liang, J.-H. Jia, X.-B. Cai, Y.-Q. Zhao, Z.-Q. Wang and C.-Z. Lu, *Inorg. Chem. Front.*, 2022, **9**, 6561–6566.
59 G. Giobbio, P. B. Coto, J.-F. Lohier, J.-L. Renaud, S. Gaillard and R. D. Costa, *Dalton Trans.*, 2024, **53**, 12307–12315.
60 A. V. Artem'ev, M. R. Ryzhikov, A. S. Berezin, I. E. Kolesnikov, D. G. Samsonenko and I. Y. Bagryanskaya, *Inorg. Chem. Front.*, 2019, **6**, 2855–2864.
61 A. Kaeser, O. Moudam, G. Accorsi, I. Séguy, J. Navarro, A. Belbakra, C. Duhayon, N. Armaroli, B. Delavaux-Nicot and J.-F. Nierengarten, *Eur. J. Inorg. Chem.*, 2014, 1345–1355.
62 R. Liu, C. Liu, J. Xiao, X. Sun, M. Yan, C. Du and B. Zhang, *Inorg. Chim. Acta*, 2024, **568**, 122108.
63 M. Z. Shafikov, R. Czerwieniec and H. Yersin, *Dalton Trans.*, 2019, **48**, 2802–2806.
64 K. Matsumoto, T. Shindo, N. Mukasa, T. Tsukuda and T. Tsubomura, *Inorg. Chem.*, 2010, **49**, 805–814.
65 S. Igawa, M. Hashimoto, I. Kawata, M. Hoshino and M. Osawa, *Inorg. Chem.*, 2012, **51**, 5805–5813.
66 M. Osawa and M. Hoshino, *Chem. Commun.*, 2008, 6384–6386.
67 M. Matejdes, M. Stöter, R. Czerwieniec, M. Leitl, S. Rosenfeldt, T. Schumacher, J. Albert, M. Lippitz, H. Yersin and J. Breu, *Adv. Opt. Mater.*, 2021, **9**, 2100516.
68 M. F. Cain, S. C. Reynolds, B. J. Anderson, D. S. Glueck, J. A. Golen, C. E. Moore and A. L. Rheingold, *Inorg. Chim. Acta*, 2011, **369**, 55–61.
69 Y. Okano, H. Ohara, A. Kobayashi, M. Yoshida and M. Kato, *Inorg. Chem.*, 2016, **55**, 5227–5236.
70 C.-W. Hsu, C.-C. Lin, M.-W. Chung, Y. Chi, G.-H. Lee, P.-T. Chou, C.-H. Chang and P.-Y. Chen, *J. Am. Chem. Soc.*, 2011, **133**, 12085–12099.
71 L. Yang, D. R. Powell and R. P. Houser, *Dalton Trans.*, 2007, 955–964.
72 R. D. Shannon, *Acta Crystallogr., Sect. A: Found. Crystallogr.*, 1976, **32**, 751–767.
73 J. V. Caspar and T. J. Meyer, *J. Phys. Chem.*, 1983, **87**, 952–957.

74 A. F. Rausch, M. E. Thompson and H. Yersin, *Inorg. Chem.*, 2009, **48**, 1928–1937.
75 P. Matyba, K. Maturova, M. Kemerink, N. D. Robinson and L. Edman, *Nat. Mater.*, 2009, **8**, 672–676.
76 Z.-P. Yang and H.-C. Su, *Adv. Funct. Mater.*, 2020, **30**, 1906788.
77 (*a*) CCDC 2406496: Experimental Crystal Structure Determination, 2026, DOI: 10.5517/ccdc.csd.cc2ls4xg; (*b*) CCDC 2425241: Experimental Crystal Structure Determination, 2026, DOI: 10.5517/ccdc.csd.cc2mdnl9; (*c*) CCDC 2406497: Experimental Crystal Structure Determination, 2026, DOI: 10.5517/ccdc.csd.cc2ls4yh.